Creep, Hysteresis, and Vibration Compensation for Piezoactuators: Atomic Force Microscopy Application

D. Croft
Department of Mechanical Engineering,
50 S. Central Campus Dr., MEB 3201,
University of Utah,
Salt Lake City, UT 84112-9208

G. Shed
Burleigh Instruments Inc.,
Fishers, NY 14453

S. Devasia
Department of Mechanical Engineering,
University of Washington,
Seattle, WA 98195-2600

This article studies ultra-high-precision positioning with piezoactuators and illustrates the results with an example Scanning Probe Microscopy (SPM) application. Loss of positioning precision in piezoactuators occurs (1) due to hysteresis during long range applications, (2) due to creep effects when positioning is needed over extended periods of time, and (3) due to induced vibrations during high-speed positioning. This loss in precision restricts the use of piezoactuators in high-speed positioning applications like SPM-based nanofabrication, and ultra-high-precision optical systems. An integrated inversion-based approach is presented in this article to compensate for all three adverse affects—creep, hysteresis, and vibrations. The method is applied to an Atomic Force Microscope (AFM) and experimental results are presented that demonstrate substantial improvements in positioning precision and operating speed. [DOI: 10.1115/1.1341197]

1 Introduction

Piezoactuators have widely been used in a variety of applications such as noise-and-vibration control, and aerospace positioning systems (see, for example [1–3]). In particular, the high-precision positioning capability of piezoactuators has been exploited in Scanning Probe Microscopy (SPM) to move sensor probes over sample surfaces while collecting nano-level, surface-property information [2]. However, the positioning precision can be significantly reduced due to nonlinear hysteresis effects when piezoactuators are used in relatively long-range, positioning applications (see, e.g. [4]). Therefore, piezoactuators are typically operated in the linear range to avoid positioning errors caused by nonlinear hysteresis effects. Another cause for loss in precision is drift due to creep effects [5,6], which become significant when positioning is required over extended periods of time, e.g., during the slow operation of a SPM. Loss of precision also occurs due to induced vibrations when the positioning bandwidth is increased relative to the first resonant vibrational frequency of the piezoactuator. This vibration-caused loss in positioning precision is typically small at low operating speeds. Therefore, the operating bandwidth is restricted to be much smaller than the first resonance frequency of the piezoactuator—typically, 10–100 times lower than the first resonance frequency in ultra-high-precision applications like SPM. Thus, hysteresis, creep, and vibration cause positioning-errors which critically limit the operating speed and range of piezoactuators, and limit the development of piezoactuator applications like high-throughput SPM-based nanofabrication [7] and high-precision positioning of optics [8]. The contribution of this article is the development of an integrated, model-based, inversion approach to compensate for all three adverse effects—creep, hysteresis and vibration. The method is applied to an Atomic Force Microscope (AFM) and experimental results are presented that demonstrate substantial improvements in positioning precision and operating speed.

High Speed Scanning Probe Microscopy. Piezoactuators are used for positioning sensor-probes in Scanning Probe Microscopy (SPM) like Atomic Force Microscopy [2]. Although SPM has improved greatly since its initial development, SPM is still relatively slow with imaging time typically ranging from several seconds to minutes. Higher-speed SPM is necessary for several applications—for example, to develop real-time SPM-imaging for semiconductor industries, to study mechanisms of fast surface processes, to develop SPM-based high-density data storage, and to develop SPM-based nanofabrication equipment [2,7,8]. A critical limitation that prevents the development of high-speed SPM is the lack of piezoactuators (at present) that can achieve high-speed, high-precision positioning (scanning) of sensor-probes across a sample surface. In this article, we study the problem of improving the scan control, which is commonly achieved by using tube-shaped piezoactuators referred to as piezoscanners [2]. In particular, we study the scan control in the x-y axes—movements in these axes are used to scan sensor-probes (in SPM) parallel to the sample surface as shown in Fig. 1. For such piezoscanners, we demonstrate significant improvements in positioning speed and precision by using model-based inversion techniques. It is noted that this effort to improve x-y axes scanning is complimentary to other works aimed at improving SPM performance such as efforts to improve z-axis positioning control (of movements perpendicular to the sample as shown in Fig. 1), and to develop high speed electronics for SPM. While the focus of this article is on SPM piezoscanners, we note that the control technique presented here is

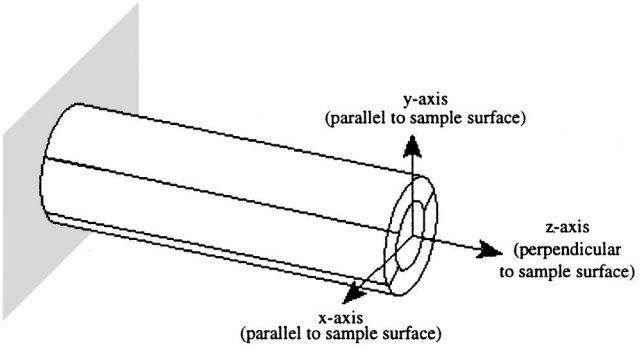

Fig. 1 x-y-z **axes of tube-shaped piezoactuator used in scanning probe microscopy**

Contributed by the Dynamic Systems and Control Division for publication in the JOURNAL OF DYNAMIC SYSTEMS, MEASUREMENT, AND CONTROL. Manuscript received by the Dynamic Systems and Control Division November 19, 1999. Associate Editor: T. Kurfess.

also applicable to other piezoactuator-based positioning systems like inchworm stages and flexural stages, and multi-probe systems.

Compensation Techniques. Nonlinear hysteresis effects can be corrected using charge control (rather than voltage control, see, e.g. [9]) and by using capacitor-insertion methods [10], which improve the linearity of the piezoactuator. However, charge-control techniques can also lead to drift and saturation problems and the capacitor insertion method can greatly reduce the range of the piezoactuator [9,10]. Another current limitation is caused by induced vibrations, which restrict the positioning bandwidth to be 10–100 times lower than the first, resonant, vibrational frequency of the piezoscanner—especially in ultra-high-precision applications like SPM. An approach to increase the positioning bandwidth is to use piezoactuators with fast dynamic response, i.e., with large vibrational-resonance frequency. For example, faster dynamic response can be achieved by using shorter piezoactuators or by using alternate designs such as piezo plate-scanners. A disadvantage with this approach is that the stiffening of the piezoactuator also tends to limit its positioning range. It is also noted that although the achievable scan rate can be larger because of larger vibrational-resonance frequencies, the positioning bandwidth is still limited by the smallest resonant frequency of the piezoactuator. Another approach is to use post-correction techniques [11] for removing creep, hysteresis and vibration effects. These post-correction methods significantly improve acquired SPM-images in metrology applications, however, such post-processing approaches cannot be used in online SPM applications such as nano-fabrication in which real-time compensation is needed.

Recent developments in precision sensors (particularly optical, capacitive, and inductive sensors) have made feedback-based control methods more feasible in SPM applications. For example, feedback-based control can be used to improve the linearity for large-range applications and to correct for low-frequency creep effects [12,13]. However, lack of sensors with sufficient resolution and bandwidth still limits the use of feedback-based control techniques in SPM applications. Further, turnaround transients in SPM applications due to velocity changes in the scan path can substantially limit the achieved maximum scan rates, and performance improvements can also be limited due to instabilities in the closed-loop system [11,14]. In this article, we develop a model-based feedforward approach to compensate for positioning distortions. This approach exploits the known dynamics to improve scanning precision and bandwidth. We note that feedback can still be used in conjunction with the proposed inversion-based method (a) to further increase positioning precision and bandwidth, and (b) to robustly account for modeling uncertainties [12,15].

Model-based inversion approaches have been used in the past to correct nonlinear hysteresis effects and, thereby, to improve positioning performance of piezoactuators at low frequencies [4]. The contribution of this article is to integrate hysteresis compensation techniques with inversion-based approaches [16–18] to achieve high-speed, high-precision positioning. In addition, creep-caused distortions are also reduced by modeling the creep dynamics as a series of viscoelastic elements [19] and then compensating for it using model-based inversion. The proposed inversion-based methodology is then applied to the piezoscanner of an Atomic Force Microscope (AFM) and experimental results demonstrate the efficacy of the method in high-speed, high-precision imaging.

The experimental modeling approach is discussed in Section 2 along with the development of the inversion-based, feedforward-compensation technique. The compensation technique is applied to an industrial AFM system and experimental results are provided in Section 3 along with discussions. Our conclusions are in Section 4.

2 Model-Based Inversion

The experimental system (see Fig. 2) studied in this article is a Burleigh Metris-2000 AFM, which uses a tube-shaped piezoscanner to position a nano-force-sensor probe [2]. The piezoscanner allows three directions of position-control—displacements parallel to the sample surface (x-y plane) and perpendicular (z-axis) to the sample surface (see Fig. 1). An optical sensor was available to measure the x-y displacements and a feedback sensor was available to measure surface-force effects along the z-axis of the piezoscanner. In this section, we describe the experimental modeling and inversion-based compensation approach for the piezo scanner. We begin by introducing the modeling and inversion approach.

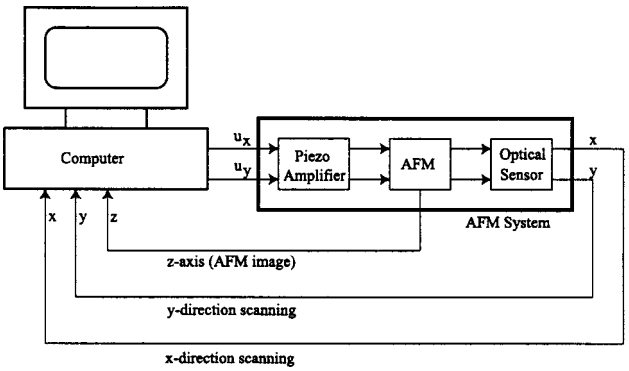

Fig. 2 Schematics of experimental AFM system

2.1 Approach to Modeling and Inversion. The piezoactuator system is modeled along each scan-axis as the cascade of hysteresis, vibration and creep sub-models as shown in Fig. 3. The axes-decoupled approach provides sufficient precision to substantially improve SPM operations (as demonstrated by experimental results in Section 3). Coupling effects between the x and y axes could be included in the modeling to achieve further increase in precision and the proposed inversion-approach can be extended to such multi-input multi-output systems [17], however, at additional modeling complexity.

In the cascade model, hysteresis is modeled as an input nonlinearity. Hysteresis has been attributed to domain switching in piezoactuators [20], which in turn affects the electromechanical coupling. For example, the mechanical strain induced in the piezoelectric actuator has been shown to be nonlinear with the applied voltage. In contrast, the induced strain has been shown to be linear with an applied charge or an external mechanical input to the piezo [9,10]. Furthermore, with the leads of the piezoactuator open, an applied mechanical input to the piezoactuator exhibits a linear input-to-displacement behavior [9]. These results suggest that hysteresis should be modeled as an input nonlinearity [9] between the applied actuator-voltage and the resulting mechanical input. As shown in Fig. 3, in the cascaded model, the input voltage u_x first passes through a hysteresis submodel H. The output of this submodel is the effective mechanical input F which actuates the mechanical-vibrational dynamics G_{sx}. The resulting displacements are then passed through a creep sub-model that modifies the resulting displacements.

The modeling and inversion approach is carried out using the following steps.

• Step 1 Model the linear creep effects: During this procedure, the inputs to the piezoactuator are kept small to operate it in the

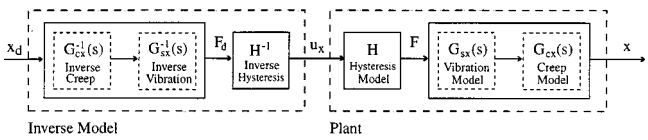

Fig. 3 Inversion-based approach for *x*-axis scan control

linear range (so hysteresis effects are negligible). The creep response is modeled over extended periods of time during which the vibrational effects are also negligible.

• Step 2 Model the linear vibrational effects: During this procedure, the inputs to the piezoactuator are still kept small to operate it in the linear range (so hysteresis effects are negligible). The vibrational response is modeled using relatively-fast, time-varying inputs—so the creep effects are small.

• Step 3 Model the nonlinear hysteresis effects: During this modeling process slowly varying inputs are used to reduce the excitation of the vibrational dynamics. However, creep effects cannot be ignored and an inverse creep model is used to isolate and study the response due to the hysteresis effect. In this step, the inverse of the hysteresis model H^{-1} is directly found.

• Step 4 Find the inverse of the vibrational dynamics: An optimal inversion approach is used for inverting the vibrational dynamics and to tradeoff large inputs with tracking precision. The three inverses of the creep, hysteresis, and vibrational sub-models are then cascaded to find the inverse for a desired output-trajectory.

Next, we present the details of the modeling and inversion process. The modeling of linear creep and vibration effects are described in Subsections 2.2 and 2.3. The inverse-hysteresis modeling is described in Subsection 2.4 followed by a description of the inversion of the vibrational dynamics in Section 2.5. The total inverse for the piezoactuator system is then found by cascading the inverse hysteresis model with the inverse of the linear dynamics (creep and vibrational dynamics) as shown in Fig. 3.

2.2 Step 1: Modeling Creep Effects. Piezoelectric creep can result in significant loss in precision, especially when operating over extended periods of time at an offset position from the center of the piezoactuator's positioning range. To isolate and model the effects of creep, the positioning range was kept small to minimize hysteresis effects. Similarly, the outputs were measured over extended periods of time (in the five minutes range) so that effects of induced vibrations can be neglected. Thus, at extremely low frequencies and relatively low-input magnitudes, the effects of vibrations and hysteresis nonlinearities are small, and the dominant effect is creep in the input-to-output response. The creep response, which occurs both in the mechanical and electrical domains, was modeled as a series connection of springs and dampers [19]. The low-frequency response of the piezoactuator was modeled as shown in Fig. 4, and can be described as

$$\frac{x(s)}{u_x(s)} = G_{\text{low}_x} = \frac{1}{k_{x_0}} + \sum_{i=1}^{n_{cx}} \frac{1}{c_{x_i} s + k_{x_i}} \tag{1}$$

where $x(s)$ is the measured response in the x-direction (in the Laplace domain) and $u_x(s)$ is the input voltage affecting the x-direction movements. In the above equation, k_{x_0} models the elastic behavior at low frequencies—it does not however, model creep or vibrational effects. Models were developed for several choices of model-order n_{cx} (i.e., numbers of spring-damper elements) and the resulting standard deviation σ_c and maximum error $E_{\max_c}$ are compared in Table 1, where the standard deviation σ_c is defined as

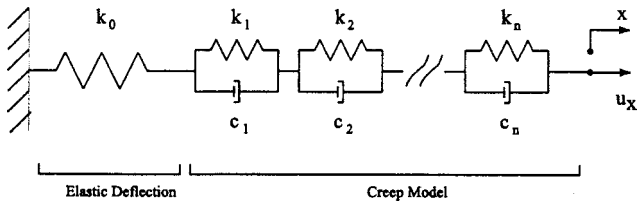

Fig. 4 Viscoelastic creep model

Table 1 Comparison of error in predicted creep response with different model-orders

n_{cx}	σ (volts)	$E_{\max}$ (volts)
1	.00729	.0468
2	.00689	.0262
3	.00652	.0231
4	.00653	.0231
5	.00652	.0224

$$\sigma_c = \sqrt{\frac{1}{N_{cx}-1} \sum_{i=1}^{N_{cx}} (x_i - \overline{x_i})^2} \quad \text{volts} \tag{2}$$

and the maximum error $E_{\max_c}$ is defined as

$$E_{\max_c} = \max_i |x_i - \overline{x_i}| \quad \text{volts.} \tag{3}$$

In the above definitions, x_i is the measured output, $\overline{x_i}$ is the predicted output from the creep model, and N_{cx} is the number of measured data points.

As seen in Table 1, modeling errors did not decrease substantially when using model orders greater than three, hence a third order model was chosen to model the creep behavior. This creep model, and comparisons with experimental results are provided in the next subsection along with the vibrational models. Creep effects in the y-axis were also modeled similarly.

2.3 Step 2: Modeling the Vibrational Dynamics. To isolate and study the response due to induced vibrations, relatively high-frequency inputs were used so that the effects of creep are negligible. The input amplitudes were also kept small so that hysteresis effects are small. The vibrational dynamics of the piezoscanner were modeled experimentally by applying a low-amplitude, sinusoidal input u_x of increasing frequency to the piezoscanner and measuring the resulting x-axis displacement (the output) using an optical sensor. A Dynamic Signal Analyzer (HP3650A) was used to study the input-output response and to construct a model of the vibrational dynamics. This model of the vibrational dynamics was integrated with the model of the creep dynamics to obtain the following input-output description of the piezoactuator's linear dynamics

$$\frac{x(s)}{u_x(s)} = G_{sx}(s) G_{cx}(s) \tag{4}$$

where the vibrational submodel is given by

$$G_{sx}(s) = \frac{.435s^3 + 3910s^2 + 1.21\times10^7 s + 1.07\times10^{14}}{s^4 + 8980s^3 + 2.78\times10^7 s^2 + 7.38\times10^{10} s + 1.55\times10^{14}} := \frac{n_{sx}(s)}{d_{sx}(s)} \tag{5}$$

and the creep submodel is given by

$$G_{cx}(s) = \frac{s^3 + .630s^2 + .0216s + 6.25\times10^{-5}}{s^3 + .516s^2 + .0171s + 4.69\times10^{-5}}. \tag{6}$$

Similarly, the y-axis linear dynamics were found as

$$\frac{y(s)}{u_y(s)} = G_{sy}(s) G_{cy}(s) \tag{7}$$

where

$$G_{sy} = \frac{.419s^3 + 3760s^2 + 1.17\times10^7 s + 1.10\times10^{14}}{s^4 + 8980s^3 + 2.78\times10^7 s^2 + 7.38\times10^{10} s + 1.55\times10^{14}} := \frac{n_{sy}(s)}{d_{sy}(s)} \tag{8}$$

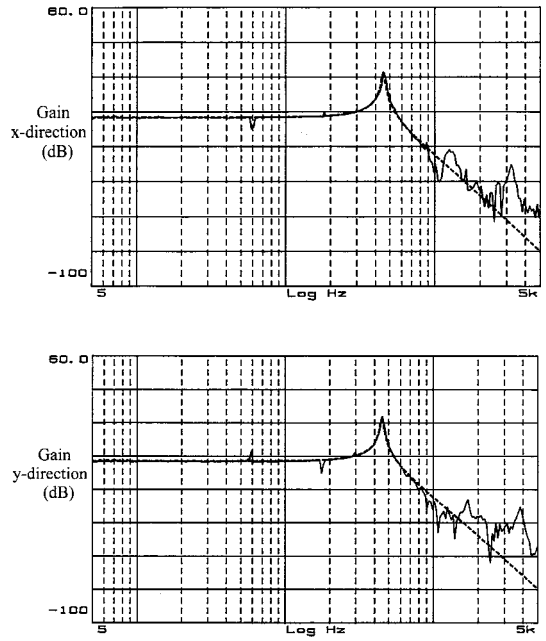

Fig. 5 Bode plots (solid line is measured and dashed line is model)

$$G_{cy}=\frac{s^3+.589s^2+.0233s+1.48\times10^{-5}}{s^3+.517s^2+.0197s+1.14\times10^{-5}}. \quad (9)$$

These equations represent the linear dynamics of the piezoscanner and effectively predict the input-output response when the positioning range is small (i.e., when the hysteresis effects are negligible). The predicted response of the models are compared with the experimental frequency response in Fig. 5, which shows that fourth order vibrational sub-models capture the vibrational dynamics relatively well up to the first resonance frequency (454 Hz). We note that the creep submodel increases the low-frequency gain of the system, and that the creep effect becomes negligible at relatively-high frequencies because G_{cx} and G_{cy} tend to 1 at high frequencies. The predicted response of the model compares well with the experimental creep response in *x*-axis as shown in Fig. 6.

2.4 Step 3: Preisach Inverse-Hysteresis Model. Once the linear creep and vibrational dynamics of the system have been determined, the hysteresis nonlinearities of the system were modeled. Rather than model the forward hysteresis model (from u_x to F in Fig. 3), and then use an iterative method to find the inverse-hysteresis model [4], we directly model the inverse hysteresis effect. The frequency of the applied input u_x to the piezoactuator was kept low for avoiding vibrations, however, creep effects could not be avoided in the measured response. The measured response x was corrected to isolate the hysteresis effects by inverting Eq. (1)

$$F_d(s)=G_{\text{low}_x}^{-1}[x(s)]. \quad (10)$$

The nonlinear inverse-hysteresis (see Figure 3) from F_d to the applied voltage u_x

$$u_x=H^{-1}[F_d] \quad (11)$$

was then modeled. The main challenge in modeling hysteresis (and inverse-hysteresis) nonlinearity is to capture the variation of the input-to-output slope. The ascending and descending curves of the hysteresis nonlinearity tend to be different and tend to be amplitude dependent. One method consists of curve-fitting separate polynomials [21] to the ascending and descending portions of the measured inverse-hysteresis data. However, when the inputs are more complex, such as an input that contains multiple frequency components or inputs with changing amplitudes, the polynomial method can lead to significant modeling errors. Another approach is to use the Coleman-Hodgdon (C-H) equations, which have been used in the past to capture hysteresis and inverse-hysteresis effects (see, for example [22]). The Coleman-Hodgdon equations generalize the polynomial-based approach and give an excellent description of the hysteresis nonlinearity for fixed-amplitude inputs—however, this approach also tends to have limited precision when the input to the hysteresis nonlinearity has amplitude variations. To capture such amplitude variations, lumped parameter models have been suggested for modeling hysteresis effects in piezoelectric scanners (see, for example [9]). This method uses a parallel connection of elasto-slide elements. Each elasto-slide element consists of an ideal spring coupled to a massless block that is subjected to Coulomb friction. The stick-slip behavior that arises from these elements is analogous to the behavior of electrical dipoles that constitute a piezoelectric material. When the piezoelectric material is subjected to an electric field, each dipole remains essentially in its original orientation until the electric field is sufficient to flip it into alignment with the field. This approach, to model the switching of fields, is generalized in the Preisach approach, which models the hysteresis effects as an infinite collection of switches [4,23,24]. The Preisach approach has been shown to be effective in capturing both the amplitude variations and nonsymmetry in the hysteresis response of piezo-actuators—the Preisach approach is used in this article to model the inverse-hysteresis effects.

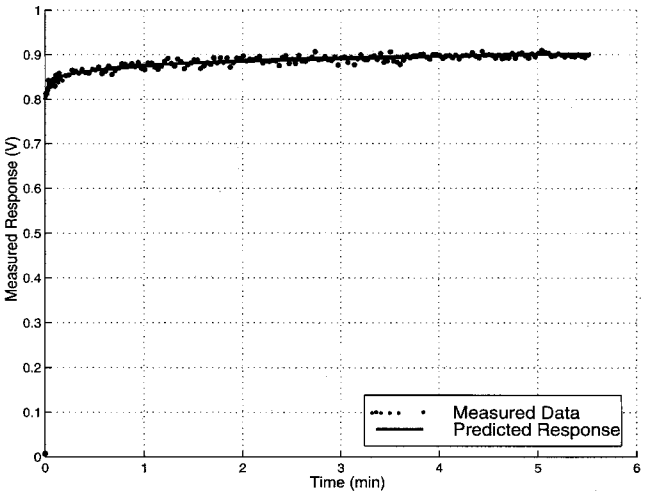

Fig. 6 Comparison of measured and predicted creep response

The Preisach inverse-model is developed using elementary inverse-hysteresis operators $\gamma_{\alpha\beta}$, which can be interpreted as two-position relays with separate *up* and *down* switching values as shown in Fig. 7. Outputs of these inverse-hysteresis operators $\gamma_{\alpha\beta}$ can assume two values, $+1$ and -1, depending on the current value and direction of the input to the operator as shown in Fig. 7(*a*). The change, Δ, in the value of the inverse-hysteresis operator $\gamma_{\alpha\beta}$ for a given F_d is defined as follows (see Fig. 7(*a*))

$$\begin{aligned}\Delta(\gamma_{\alpha\beta},F_d)&=+2 \text{ if } F_d\geqslant\alpha \text{ and } \gamma_{\alpha\beta}=-1\\ &=-2 \text{ if } F_d\leqslant\beta \text{ and } \gamma_{\alpha\beta}=+1\end{aligned} \quad (12)$$

with $\gamma_{\alpha\beta}=-1$ at the start [24]. The net effect of all these individual inverse-hysteresis operators is represented as the superposition of an infinite collection of the individual inverse-Preisach operators [24]

$$u_x(t)=\int\int_{\alpha\geqslant\beta}\mu(\alpha,\beta)\gamma_{\alpha\beta}[F_d]d\alpha d\beta \quad (13)$$

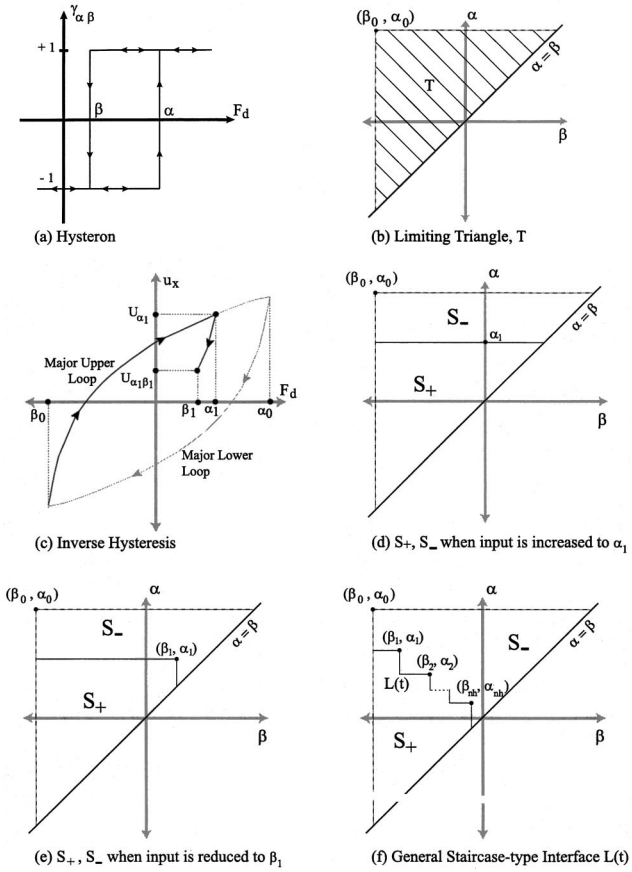

Fig. 7 Preisach inverse-hysteresis model

where $F_d(t)$ is the input to the inverse-Preisach model, $u_x(t)$ is the output of the inverse-Preisach model, $\mu(\alpha,\beta)$ is the inverse-Preisach weighting function, α and β are the *up* and *down* switching values of the elementary inverse hysteresis operator (see Fig. 7(*a*)), and $\gamma_{\alpha\beta}$ is the elementary inverse-hysteresis operator (called the hysteron). The weighting function $\mu(\alpha,\beta)$ associated with the hysteron $\gamma_{\alpha\beta}$ can be either positive or negative. This weighting function $\mu(\alpha,\beta)$ must be determined before the above inverse-hysteresis model can be implemented—the determination of the weighting function is discussed next.

We begin by presenting a geometric representation of the inverse-hysteresis operator. It will be assumed that the hysteresis nonlinearity operates within closed major loops [24] and therefore the inverse-Preisach weighting function $\mu(\alpha,\beta)$ has a compact support, i.e., $\mu(\alpha,\beta)$ is zero outside a bounded region. This region is the right-angled triangle T shown in Fig. 7(*b*) with its hypotenuse on the line $\alpha=\beta$ and with the point (β_0,α_0) as the vertex of its right angle. In general, the triangle T can be separated into two regions S_+, where $\gamma_{\alpha\beta}=+1$ and S_- where $\gamma_{\alpha\beta}=-1$. For example, if the output of the model is at the lower saturation value then $\gamma_{\alpha\beta}=-1$ for the entire triangle (i.e., region S_- is the entire triangle). Now, let the input to the model be monotonically increased from the negative saturation value β_0 to some arbitrary value α_1, as shown in Fig. 7(*c*)—let the corresponding output of the inverse-hysteresis operator be U_{α_1}. With this input to the model, all hysteresis operators $\gamma_{\alpha\beta}$ with ascending switching values $\alpha\leqslant\alpha_1$ will be in the upper switched value of $+1$. This corresponds to the limiting triangle T being split into two (S_+ and S_-) as shown in Fig. 7(*d*). Next, let the input to the inverse-operator be monotonically decreased to some arbitrary value β_1—let the corresponding output of the inverse-hysteresis operator be $U_{\alpha_1\beta_1}$ (see Fig. 7(*c*)). Now, all hysteresis operators $\gamma_{\alpha\beta}$ in the previous S_+ (Fig. 7(*d*)) with $\beta\geqslant\beta_1$ will switch back to the lower value of -1 as shown in Fig. 7(*e*) which also shows the new S_+ and S_- regions. In general, at any time t, the two regions $S_+(t)$ and $S_-(t)$ where $\gamma_{\alpha\beta}$ is positive and negative, respectively, are separated by a staircase-type interface $L(t)$ whose vertices are local maxima and minima of previous inputs to the inverse-hysteresis model (as shown in Fig. 7(*f*)). Note that all prior maxima and minima of the input to the inverse-hysteresis operator are not represented by $L(t)$ because some of the previous maxima and minima might be wiped out. In particular, each local maximum wipes out all vertices whose α coordinates are below this maximum, and each local minimum wipes out the vertices whose β coordinates are above this minimum [24]. Next, the inverse-hysteresis operator (Eq. (13)) is rewritten as

$$u_x(t)=\int\int_{S_+(t)}\mu(\alpha,\beta)d\alpha d\beta-\int\int_{S_-(t)}\mu(\alpha,\beta)d\alpha d\beta. \tag{14}$$

Let $\Gamma_{\alpha_1\beta_1}$ be the difference (in area) between the S_+ regions in Figs. 7(*d*) and 7(*e*). Then we get the following relationship between μ and the corresponding output values U_{α_1} and $U_{\alpha_1\beta_1}$

$$U(\alpha_1,\beta_1):=\frac{U_{\alpha_1}-U_{\alpha_1\beta_1}}{2}=\int\int_{\Gamma_{\alpha_1\beta_1}}\mu(\alpha,\beta)d\alpha d\beta$$

$$=\int_{\beta_1}^{\alpha_1}\left(\int_{\beta_1}^{y}\mu(x,y)dx\right)dy,$$

which can be used to find the inverse-Preisach weighting function $\mu(\alpha,\beta)$, for general α and β with $\alpha\geqslant\beta$, as [24]

$$\mu(\alpha,\beta)=-\frac{\partial^2U(\alpha,\beta)}{\partial\alpha\partial\beta} \tag{15}$$

where

$$U(\alpha,\beta):=\frac{U_\alpha-U_{\alpha\beta}}{2} \tag{16}$$

and U_α and $U_{\alpha\beta}$ are found using the limiting ascending branch (e.g., as shown in Fig. 7(*c*) for U_{α_1} and $U_{\alpha_1\beta_1}$). Although the inverse-model can be implemented using Eq. (14), we note that the direct application of the above method encounters two main difficulties. First, the determination of the Preisach weight function $\mu(\alpha,\beta)$ requires the differentiation of experimentally measured data (Eq. (15)), which may strongly amplify noise in the data, leading to errors. Second, the method (in Eq. (14)) is time consuming, which impedes the use of the Preisach model in online implementation [24]. Therefore, the Preisach model was implemented in a modified form (referred to as the numerical Preisach model) which involves only measured experimental data [24]. The numerical inverse-hysteresis model can be obtained by rewriting Eq. (14) using the staircase boundary function $L(t)$ shown in Fig. 7(*f*) as

$$u_x(t)=-U(\alpha_0,\beta_0)+2\sum_{k=1}^{nh}\left[U(\alpha_k,\beta_{k-1})-U(\alpha_k,\beta_k)\right] \tag{17}$$

where $\{\alpha_k\}$ and $\{\beta_k\}$ are decreasing and increasing sequences of α and β coordinates of interface $L(t)$ vertices, respectively, as shown in Fig. 7(*f*) and *nh* is the number of horizontal links in the interface $L(t)$. When implementing Eq. (17), we note that experimental data for $U(\alpha,\beta)$ could be collected for a finite number of α and β values in the triangle T, and $U(\cdot,\cdot)$ at other points in the triangle T can be computed using interpolation. For example, in our system, the applied voltage to the system was varied between

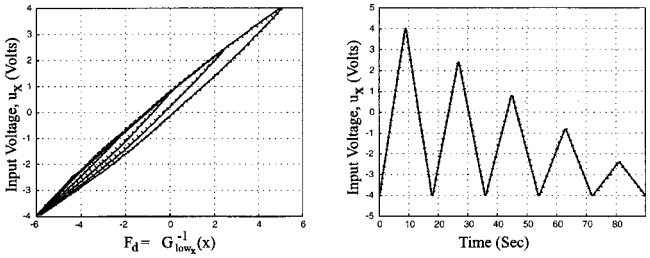

Fig. 8 Experimental verification of inverse-hysteresis model: The predicted input (solid line) from the inverse-hysteresis model is compared with the actual input (dotted line) applied to the system.

± 4 V—the corresponding variation of the input F_d to the inverse model was between -5.9492 V and 5.1373 V. The experimental data was used to find $U(\alpha,\beta)$ in the inverse model at fifty-one evenly-spaced values of, each, α and β ($\alpha \geqslant \beta$) with the same range as F_d, i.e., between -5.9492 V and 5.1373 V. Further computational and implementation issues in the Preisach approach can be found in Refs. [23] and [25].

The inverse-hysteresis model was verified experimentally and results are shown in Fig. 8. The standard deviation of the error σ_H in the predicted response of the inverse-hysteresis model was

$$\sigma_H = \sqrt{\frac{1}{N_H - 1}\sum_{i=1}^{N_H}(u_{xi} - \overline{u_{xi}})^2} = 0.0416 \text{ volts} \tag{18}$$

and the maximum error $E_{\max_H}$ was

$$E_{\max_H} = \max_i(|u_{xi} - \overline{u_{xi}}|) = .118 \text{ volts} \tag{19}$$

where u_{xi} is the voltage applied to the piezoactuator, and $\overline{u_{xi}}$ is the predicted applied-voltage obtained by using the inverse hysteresis model when $F_d(s) = G^{-1}_{\text{low}_x}[x(s)]$ was used as an input to the inverse-hysteresis model. In the above expressions, N_H is the number of measured data points.

2.5 Step 4: Inversion of Vibrational Dynamics. An inversion-based approach [16] can be used to determine the vibration-compensating input u_{xd} that achieves tracking of a desired scan trajectory x_d (i.e., the output trajectory) by inverting the vibrational dynamics (Eq. (5)) to obtain

$$u_{xd}(j\omega) = G^{-1}_{sx}(j\omega)x_d(j\omega) = \frac{d_{sx}(j\omega)}{n_{sx}(j\omega)}x_d(j\omega). \tag{20}$$

The exact-output tracking input, found from Eq. (20), is *unique*. However, for a generic desired output-trajectory, this exact-tracking input might depolarize the piezoactuator or saturate the piezo-amplifier. The input might also excite unwanted resonances in the structure that houses the piezoactuator. Further, the input-bandwidth needed to achieve this output trajectory might also be unavailable. Therefore, an optimal inverse approach is used (a) to generate a modified output trajectory, and (b) to find the input needed to achieve tracking of this new output trajectory. We note that desired output-trajectories are typically chosen in an ad-hoc manner. For example, the output is often chosen as a triangular to-and-fro scan in SPM. These triangular scans cannot be tracked exactly because the velocities are discontinuous at the corners leading to infinite accelerations, and therefore, the corners need to be smoothed for achieving tracking. The optimal inverse approach allows the systematic *smoothing* of the desired output-trajectory. The optimal inverse can also be used to trade off the tracking requirement for achieving other goals such as reduction of the input bandwidth and amplitude, and for reducing the effects of model uncertainties. We formulate this optimal inversion problem as the minimization of a quadratic cost functional of the type

$$J(u) = \int_{-\infty}^{\infty}\{u^*(j\omega)R(j\omega)u(j\omega) + [x(j\omega) - x_d(j\omega)]^*Q(j\omega) \times [x(j\omega) - x_d(j\omega)]\}d\omega. \tag{21}$$

The superscript * implies conjugate transpose, and x_d is the desired output trajectory (scan path) in the frequency domain. The above objective function is formulated for inverting the vibrational dynamics in the x-axis direction—a similar approach was followed for inverting the y-axis vibrational dynamics.

In the above objective functional, $R(j\omega)$ and $Q(j\omega)$ are non-negative frequency dependent real-valued scalars (both should not be simultaneously zero at any frequency) that represent the weights on input u and output-tracking-error $(x - x_d)$. For example, the amplitudes of the inputs can be reduced by choosing large values of R. This, however, can result in greater tracking error $(x - x_d)$—see [17] for more discussion on these trade-offs. However, we point out two cases with extreme choices of R and Q. In the first case, if the weight on the scan-path tracking error is zero, $Q = 0$, but R is nonzero, then the best strategy is not to track the desired trajectory at all. This can be used if modeling errors are large, for example at frequencies substantially higher than the first resonance frequency of the piezoactuator (see Bode Plots in Fig. 5). Similar frequency-dependent weights on the input and output-error can be used, for example, to account for actuator-bandwidth limitations. In the second case, if the weight on the inputs are zero, i.e., $R = 0$ but Q is nonzero then the best strategy is to exactly track the desired scan-path, i.e., $x(j\omega) = x_d(j\omega)$. Thus, for the second case, the resulting optimal inverse is the exact-inverse input, which achieves exact-tracking of the desired scan path $x(j\omega) = x_d(j\omega)$.

The optimal input trajectory is given by the following lemma—a generic result for linear time-invariant systems can be found in [17]. Online implementation issues using preview-based inversion can be found in [26], and extensions to actuator-redundant and actuator-deficient systems can be found in [27].

Lemma. The optimal inverse input trajectory u_{opt}, to the piezo-scanner is given as

$$u_{\text{opt}}(j\omega) = \frac{d_{sx}(j\omega)}{n_{sx}(j\omega)}\left\{\frac{n^*_{sx}(j\omega)Q(j\omega)n_{sx}(j\omega)}{d^*_{sx}(j\omega)R(j\omega)d_{sx}(j\omega) + n^*_{sx}(j\omega)Q(j\omega)n_{sx}(j\omega)}\right\}x_d(j\omega) = \hat{G}^{-1}_{sx}(j\omega)x_d(j\omega). \tag{22}$$

Proof: The cost functional (Equation 21) can be rewritten as

$$J(u) = \int_{-\infty}^{\infty}\left\{\begin{array}{l}\left[u - \dfrac{d}{n}\left(\dfrac{n^*Qn}{d^*Rd + n^*Qn}\right)x_d\right]^*\left(\dfrac{d^*Rd + n^*Qn}{d^*d}\right)\left[u - \dfrac{d}{n}\left(\dfrac{n^*Qn}{d^*Rd + n^*Qn}\right)x_d\right] \\ + \text{terms without } u\end{array}\right\}dw$$

where the explicit dependence on $j\omega$ and the subscript sx are not written for ease in notation. The lemma follows by setting the quadratic term to zero. □

The optimal-inverse input u_{opt} is then applied to the piezoscanner for reducing the effects of vibrations and thereby for achieving high-speed scanning. The total inverse input u_x is found as the cascade of the hysteresis, creep, and vibration inverses as

$$u_x = H^{-1}\hat{G}_{sx}^{-1}G_{cx}^{-1}[x_d]. \tag{23}$$

This inversion-based approach is applied to the AFM piezoscanner in the next section.

3 Experimental Results and Discussion

To demonstrate the efficacy of the inversion-based approach, the AFM was used to image a chrome-on-glass grating (with 16 μm spacing) in two sets of experiments. The first set of experiments was performed at low scanning speeds to study the effects of hysteresis and creep and the results are shown in Fig. 9. In this first set of experiments, the scan rates were low and, therefore, the vibrational effects were negligible. The second set of experiments was performed at higher scan-rates to demonstrate the effective reduction of all the three adverse effects—hysteresis, creep, and induced vibration. The experimental results are shown in Figs. 10–12. As in standard SPM practice, z-axis feedback was used to initially position the sensor-probe close to the sample surface. However, the z-axis feedback was then kept inactive (at relatively low feedback gain) to isolate and study the effectiveness of the model-based compensation techniques for high-speed positioning in the x-y axes. All the experiments were conducted with the same setup.

3.1 Creep and Hysteresis Effects. In the first set of experiments, the AFM was used to image the chrome grating at low scan rates (1 Hz). A sequence of four inputs were applied. First, an input without inverse-compensation was applied to the AFM (Fig. 9(*a*)). Second, an inverse-input that compensated for creep effects (but not the hysteresis) was applied to the AFM (Fig. 9(*b*)). For the third case, an input that compensated for hysteresis effects only (and not creep effects) was applied to the AFM (Fig. 9(*c*)). For the fourth case, the complete inverse was used (see Fig. 9(*d*)).

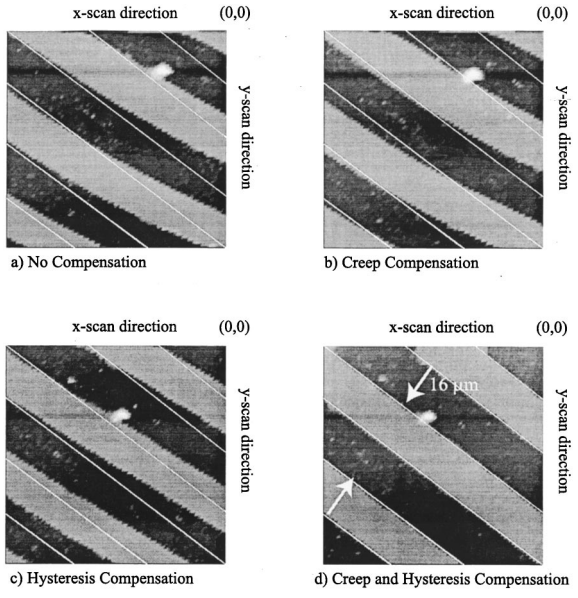

Fig. 9 Compensation of creep and hysteresis effects at 1 Hz scanning. Parallel white lines are markers for comparison between plots.

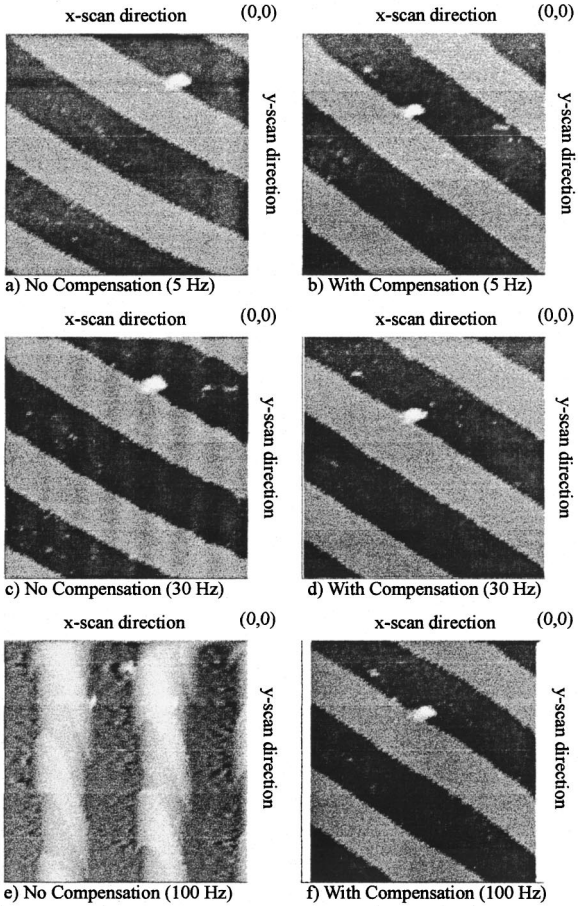

Fig. 10 High speed compensation of plezoactuator dynamics

In all the images shown in Fig. 9, the initial position of the scan (the top right corner in the images) is the zero-displacement position of the piezoscanner. The images were acquired by back-and-forth scanning in the x-axis while incrementing the y-position after each back-and-forth scan in the x-direction. Data were only collected when the x-position was increasing and were not collected in the return scan (i.e., when x-position was decreasing). The true images should show the gratings relatively parallel and separated from each other at 16 microns. Without the inverse compensation, the image (see Fig. 9(*a*)) is distorted due to hysteresis and creep effects—the image of the grating lines have a distinct curvature. The image in Fig. 9(*a*) obtained without inverse compensation has also shifted to the right and upward compared to the image with inverse compensation shown in Fig. 9(*d*)—note that the large, lighter-colored dust-particle in Fig. 9(*d*) has shifted from near the center of the image towards the upper right-hand

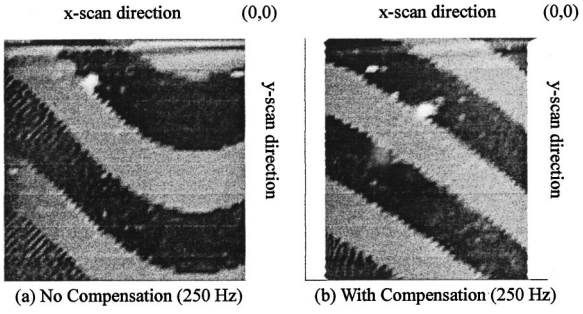

Fig. 11 Experimental results with 250 Hz scan rate

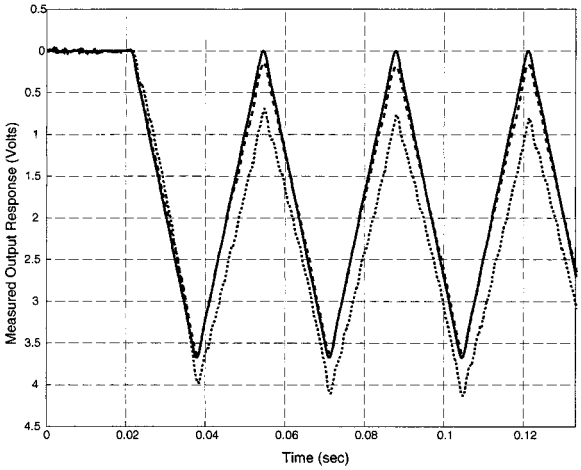

Fig. 12 Experimental results: scan-path tracking at 30 Hz showing drift due to creep, offset due to hysteresis, and oscillations due to induced vibrations (solid line represents the desired output and the light dotted-line represents tracking without inverse compensation). These effects are removed with inverse compensation (heavy dotted-line).

corner in Fig. 9(*a*). In addition, the area scanned in Fig. 9(*a*) is larger than the area scanned in Fig. 9(*d*) since four grating lines are visible in Fig. 9(*a*) and only three grating lines are visible in Fig. 9(*d*).

The major cause of the shift to the image to the right is the hysteresis effect. Note that the initial scanned line (from the top right to the top left) in Fig. 9(*a*) starts with a relatively dark segment (as in Fig. 9(*d*)). This shows that the scan without the inverse compensation starts from the same spot, however, the piezoactuator over-scans and fails to return by the same distance in the *x*-direction due to hysteresis effects. Thus, the second scanned line in the image is a light-colored area in Fig. 9(*a*). This distortion in the second scanned line is mainly due to the hysteresis effects as the creep effects are small during the relatively-short time-interval of a single to-and-fro scan. This shift of the image to the right in the second scanned line is mostly eliminated when hysteresis compensation is added (see Fig. 9(*c*)) and the area around the origin (0,0) is relatively dark. In contrast, this shift to the right of the image near the origin is not compensated when creep effects are compensated—the second scanned line is still shifted in Fig. 9(*b*).

When the hysteresis effects are compensated, the effects of creep become dominant as shown in Fig. 9(*c*). Note that in the hysteresis-compensated image (Fig. 9(*b*)), the image in the area around the origin matches the image in the corresponding area in Fig. 9(*d*) with the inverse compensation. However, creep effects tend to add a drift in the piezo-positioning. Thus, the net *y*-axis displacement is larger than the expected *y*-axis displacement. This increase in the scanned area can be seen in Figs. 9(*a*) and 9(*c*). It is noted that there is a similar creep effect in the *x*-direction but the creep effect is smaller due to the back-and-forth scanning in the *x*-direction (in contrast to the continuously increasing *y*-direction positioning). This disparity in the creep effects in *x* and *y* scans leads to the distortions in the image—the gratings curve upwards in Fig. 9(*c*) when the image is plotted on the expected scan area. Note that the addition of creep-compensation in Fig. 9(*b*) significantly reduces the drift effects and the scanned area is similar to that in Fig. 9(*d*) (although the image in Fig. 9(*b*) is shifted to the right due to hysteresis effects).

The distortions due to creep and hysteresis have been effectively removed with the inversion-based approach (shown in Fig. 9(*d*). We note that both the nonlinear hysteresis effects and the linear creep effects have to be compensated for achieving precision scanning. At this relatively-low scan rate, the vibrational effects were not significant—vibrational effects are studied next.

3.2 Vibration Effects. The acquired images with high scan rates are shown in Figs. 10 and 11. The images to the left do not have the inversion-based compensation, while the images to the right are obtained using the inversion-based compensation.

At relatively low scan rates, the vibrational effects are negligible and the main cause of image distortions is creep and hysteresis effects—as seen in the 5 Hz (scan-frequency) image obtained without compensation (Fig. 10(*a*)). When the scan rate is increased to 30 Hz, ripples appear in the image obtained without inverse-compensation (Fig. 10(*c*)), due to induced vibrations. These induced vibrations in the achieved *x*-axis can be seen in the measured *x*-displacements shown in Fig. 12. In this figure, the shift in the *x*-axis scanning due to hysteresis is also seen when the input without inversion-based compensation is applied. The second scanned line does not start from the $x=0$ position (in Fig. 12) leading to a shift in the scanned image to the right (seen in Fig. 10(*c*)). When inversion-based compensation is used, the shift in the scan path is removed—the second scan is closer to $x=0$ with inverse compensation, and output tracking is improved (see Fig. 12). The shift to the right is reduced in the resulting image (Fig. 10(*d*)). The ripples due to induced vibrations in Figure 10(*c*) are also not seen in Fig. 10(*d*) when inverse compensation is used.

As the scan rate is increased further (Figs. 10(*e*) and 11(*a*)), induced vibrations lead to severe distortions in the acquired image. In all these images, the distortions or ripples in the image caused by vibrations correspond to the first natural frequency of the scanner at 454 Hz (see Bode plot in Fig. 5). In contrast to the significant distortions in the *x*-axis scanning, the *y*-axis vibrations are not significant and do not cause image distortions because the *y*-direction movements are relatively slow. The vibration-caused distortions are significantly reduced in all the images with the addition of inversion-based compensation. In addition, scan rates have been increased to 100 Hz (Fig. 10(*f*)). Even at 250 Hz, which is over 1/2 the fundamental vibrational frequency (454 Hz), there was substantial improvement in the acquired image (compare the images in Fig. 11 obtained with and without inverse compensation)—the reduction of the scan range in the *x*-direction in Fig. 11(*b*) is due to the optimal *smoothing* of the scan path when finding the inverse of the vibrational dynamics. This reduction in range depends on the choice of the cost functional (Eq. (21)) that is used to invert the vibrational dynamics—it can be alleviated (if needed) either by re-scaling the inverse of the vibrational dynamics or by choosing a different cost functional. The experimental results presented above demonstrate that the inversion-based approach can be used to substantially improve SPM imaging at significantly-higher scan rates by compensating for creep, hysteresis and vibration effects.

We note a few issues in further increasing the scan rate. Effects of the high frequency dynamics can be seen in the high-scan rate images—these effects appear as relatively high-frequency ripples (seen in the relatively darker areas of Fig. 11). Although the effects of the *z*-axis dynamics (with resonance around 200 kHz) were not significant in the current study, these effects will become significant as the *x*-*y* axes scan rates are increased further, and faster *z*-axis controllers will become necessary. The development of high-speed *z*-axis controllers to further extend the *x*-*y* scan rates is currently under study. Another issue is the coupling dynamics between the different axes, which will become significant at higher scan rates. These coupling effects can be compensated using the proposed inversion-based approach, however, at increased modeling complexity. We also note that the current inversion based approach relies on an accurate model of the piezo positioner. Therefore, at present, a limitation to increasing the scan rate and precision in the AFM piezoscanner is modeling error. It is expected, that with increased modeling accuracy, the scan rate and precision could be increased further. Current efforts are also aimed at (a) integrating the inversion-based approach

with adaptive controllers using online identification of system parameters, and (b) online implementation of the inversion-based method for use in nanotechnology applications.

4 Conclusion

This article studied the ultra-high-precision positioning with piezoactuators using a model-based inversion technique. The inversion-based approach was used to compensate for loss of precision due to hysteresis during long range applications, due to creep effects during positioning over extended periods of time, and due to induced vibrations during high-speed positioning. The method was applied to an Atomic Force Microscope (AFM) and experimental results were presented that demonstrated substantial improvements in positioning precision and operating speed.

Acknowledgment

Financial support from NSF Grants CMS 9813080 and DMII 9612300 is gratefully acknowledged.

References

[1] Choi, S., Cho, S., and Park, Y., 1999, ''Vibration and position tracking control of piezoceramic-based smart structures via qft,'' ASME J. Dyn. Syst., Meas., Control, **121**, pp. 27–33.
[2] Wiesendanger, R., 1994, *Scanning Probe Microscopy and Spectroscopy*, Cambridge University Press, Cambridge, UK.
[3] Barrett, R., 1994, ''Active plate and missile wing development using directionally attached piezoelectric elements,'' AIAA J., **32**, No. 3, Mar., pp. 601–609.
[4] Ge, P., and Jouaneh, M., 1996, ''Tracking control of a piezoceramic actuator,'' IEEE Trans. Control Syst. Technol., **4**, No. 3, pp. 209–216.
[5] Robinson, R. S., 1996, ''Interactive computer correction of piezoelectric creep in scanning tunneling microscopy images,'' J. Comput.-Assist. Microsc., **2**, No. 1, pp. 53–58.
[6] Fett, T., and Thun, G., 1998, ''Determination of room-temperature tensile creep of pzt,'' J. Mater. Sci. Lett., **17**, No. 22, pp. 1929–1931.
[7] Xie, W., Dai, X., Xu, L. S., Allee, D. A., and Spector, J., 1997, ''Fabrication of cr nanostructures with scanning tunneling microscope,'' Nanotechnology, **8**, No. 2, pp. 88–93.
[8] Basedow, R. W., and Cocks, T. D., 1980, ''Piezoelectric ceramic displacement characteristics at low frequencies and their consequences in fabry-perot interferometry,'' J. Phys. E, **13**, pp. 840–844.
[9] Goldfarb, M., and Celanovic, N., 1997, ''A lumped parameter electromechanical model for describing the nonlinear behavior of piezoelectric actuators,'' ASME J. Dyn. Syst., Meas., Control, **119**, Sept., pp. 478–485.
[10] Kaizuka, H., 1989, ''Application of capacitor insertion method to scanning tunneling microscopes,'' Rev. Sci. Instrum., **60**, No. 10, pp. 3119–3122.
[11] Barrett, R. C., and Quate, C. F., 1991, ''Optical scan-correction system applied to atomic force microscopy,'' Rev. Sci. Instrum., **62**, pp. 1393–1399.
[12] Daniele, A., Salapaka, S., Salapaka, M. V., and Dahleh, M., 1999, ''Piezoelectric scanners for atomic force microscopes: Design of lateral sensors, identification and control,'' *Proceedings of the American Control Conference*, San Diego, CA, June, pp. 253–257.
[13] Cruz-Hernandez, J. M., and Hayward, V., 1997, ''On the linear compensation of hysteresis,'' *Proceedings of the 36th Conference on Decision and Control*, San Diego, CA, Dec., pp. 1956–1957.
[14] Main, J. A., and Garcia, E., 1997, ''Piezoelectric stack actuators and control system design: Strategies and pitfalls,'' J. Guid. Control Dyn., **20**, No. 3, May–June, pp. 479–485.
[15] Zhao, Y., and Jayasuriya, S., 1995, ''Feedforward controllers and tracking accuracy in the presence of plant uncertainties,'' ASME J. Dyn. Syst., Meas., Control, **117**, No. 4, pp. 490–495.
[16] Bayo, E., 1987, ''A finite-element approach to control the end-point motion of a single-link flexible robot,'' J. Rob. Syst., **4**, No. 1, pp. 63–75.
[17] Dewey, J. S., Leang, K., and Devasia, S., 1998, ''Experimental and theoretical results in output-trajectory redesign for flexible structures,'' ASME J. Dyn. Syst., Meas., Control, **120**, No. 4, Dec., pp. 456–461.
[18] Croft, D., and Devasia, S., 1999, ''Vibration compensation for high speed scanning tunneling microscopy,'' Rev. Sci. Instrum., **70**, No. 12, Dec., pp. 4600–4605.
[19] Malvern L. E., 1969, *Introduction to the Mechanics of a Continuous Medium*, chapter 6, Prentice-Hall, Englewood Cliffs, NJ, pp. 313–319.
[20] Chen, P. J., and Montgomery, S. T., 1980, ''A macroscopic theory for the existence of the hysteresis and butterfly loops in ferroelectricity,'' Ferroelectrics, **23**, pp. 199–208.
[21] Holman, A. E., Scholte, P. M. L. O., Chr. Heerens, W., and Tunistra, F., 1995, ''Analysis of piezo actuators in translation constructions,'' Rev. Sci. Instrum., **66**, No. 5, May, pp. 3208–3215.
[22] Coleman, B. D., and Hodgdon, M. L., 1986, ''A constitutive relation for rate-independent hysteresis in ferromagnetically soft material,'' Int. J. Eng. Sci., **24**, No. 6, pp. 897–919.
[23] Schafer, J., and Janocha, H., 1995, ''Compensation of hysteresis in solid-state actuators,'' Sens. Actuators A, **49**, pp. 97–102.
[24] Mayergoyz, I. D., 1991, *Mathematical Models of Hysteresis*, Springer-Verlag.
[25] Sasada, I., Urabe, H., and Harada, K., 1988, ''Hysteresis error correction of magnetic sensors using preisach model,'' IEEE Transl. J. Magn. Jpn., **3**, No. 7, pp. 586–587.
[26] Zou, Q., and Devasia, S., 1999, ''Preview-based stable-inversion for output tracking,'' ASME J. Dyn. Syst., Meas., Control, **121**, No. 4, Dec., pp. 625–630.
[27] Brinkerhoff, R., and Devasia, S., 2000, ''Output tracking for actuator deficient/redundant systems: Multiple piezoactuator example,'' J. Guid. Control Dyn., **23**, No. 2, Mar.-Apr., pp. 370–373.